International Communications in Heat and Mass Transfer 152 (2024) 107317

Contents lists available at ScienceDirect

International Communications in Heat and Mass Transfer

journal homepage: www.elsevier.com/locate/ichmt

An improved numerical model based on the equivalent thermal conductivity method for downhole thermal management systems

Jiale Peng [a], Wei Lan [a], Chao Deng [a], Fulong Wei [a], Siqi Ding [a], Run Hu [a], Bofeng Shang [b,*], Xiaobing Luo [a,*]

[a] School of Energy and Power Engineering, Huazhong University of Science and Technology, Wuhan, China
[b] School of Physics and Microelectronics, Zhengzhou University, Zhengzhou, China

ARTICLE INFO

Keywords:
Downhole thermal management system
Numerical model
Equivalent thermal conductivity
Computational accuracy
Computational efficiency

ABSTRACT

The electronics in logging tools are susceptible to thermal failure due to the extreme thermal environment. Passive thermal management system (PTMS) has been proven to protect the electronics for several hours. In this paper, a numerical model based on the equivalent thermal conductivity method was developed to determine the transient temperature of downhole electronics. Compared with the traditional analytical model or numerical model considering only one single heat transfer process, the complex heat transfer in the logging tool were comprehensively considered through the proposed model. Briefly, the heat transfer processes in the vacuum bottle were theoretically calculated rather than empirically acquired, and the convective and radiative heat transfer inside the vacuum bottle was equated to the temperature-dependent thermal conductivity of air. In addition, the proposed numerical model was compared with experiments and previous numerical models to verify the accuracy of the model, and the temperature deviation of the electronics was within 5 °C. Moreover, the computational time was greatly reduced compared with the traditional three-dimensional numerical simulation process while ensuring the accuracy of calculation. Therefore, the proposed numerical model achieved both computational accuracy and efficiency, which was expected to be widely used in the development of PTMS for logging tools.

1. Introduction

Due to the increasing demand for fossil energy sources around the world, deeper and hotter wells are becoming more attractive and economical [1–5]. Companies in oil fields around the world are exploring deep-well oil logging technology. The downhole temperature may exceed 200 °C due to the increasing exploitation depth [6]. However, the internal thermal sensitive electronics of logging tools cannot withstand such high temperatures during the detecting process for several hours, thus leading to damage or serious accidents [7–9]. Therefore, an effective thermal management system is necessary to protect the safe and stable operation of the internal electronics in logging tools [10,11].

Currently, the thermal management system for downhole electronics mainly includes active thermal management systems (ATMS) and passive thermal management systems (PTMS) [12]. The basic principle of ATMS was transporting the heat generated by the electronics to the high-temperature downhole environment, which can be categorized into vapor compression refrigeration [13–15], thermoelectric refrigeration [16–19], thermoacoustic refrigeration [20,21], Stirling refrigeration [22,23], etc. Verma et al. [13] conducted experimental tests on a vapor compression refrigeration system, and the results showed that the system was capable of transferring 175 W and 100 W of heat at ambient temperatures of 200 °C and 205 °C, respectively. Holbein et al. [14] explored thoroughly the parametric design of the components of a downhole vapor compression refrigeration system and concluded that the system is conceptually capable of sustained operation at 200 °C without time limitations. Wei et al. [15] proposed an active cooling system for downhole electronics, and the results showed the temperature of electronics was reduced to below 163 °C in the 200 °C downhole environment. However, vapor compression refrigeration systems are unreliable in high-temperature, vibrating downhole environments, making them difficult to use in logging applications. Sinha et al. [16] proposed the downhole "thermoelectric-adsorption" system. The experimental results showed that the overall cooling coefficient of performance (COP) was 0.2, with a refrigeration power of 4 W. Weerasinghe et al. [17] constructed a heat transfer model of a high-

* Corresponding authors.
E-mail addresses: shangbofeng@zzu.edu.cn (B. Shang), luoxb@hust.edu.cn (X. Luo).

https://doi.org/10.1016/j.icheatmasstransfer.2024.107317

Nomenclature

$q_{radiation,i}$	Heat flow of radiative heat transfer between neighboring reflective screens (W/m^2)
$q_{gas,i}$	Heat flow of thermal conduction of the residual gas in two adjacent layers (W/m^2)
T	Temperature (K)
T_h	Hot side temperature of vacuum layer (K)
T_c	Cold side temperature of vacuum layer (K)
R	Gas constant (R = 8.314 J/(mol·K))
ε	Surface emissivity
γ	Ratio of specific heat
σ	Stefan-Boltzmann constant ($\sigma = 5.67 \times 10^{-8}$ W/(m^2·K^4))
M	Molar mass of air (M = 29 g/mol)
P	Pressure between layers (Pa)
B	Thermal adaptation coefficient of air (B = 0.85)
C	Empirical constant (C = 0.008)
k_{spacer}	Thermal conductivity of spacer (W/(m·K))
f	Sparsity of the spacer
D_i	Thickness of i$_{th}$ spacer(m)
δ_{vacuum}	Thickness of vacuum layer (m)
k_{eff_vacuum}	Equivalent thermal conductivity of the vacuum layer (W/(m·K))
k_{air}	Thermal conductivity of air (W/(m·K))
h_c	Natural convection heat transfer coefficient of the annular space (W/(m^2·K))
R_t	Radius of skeleton of the logging tool (m)
R_f	Radius of inner wall of vacuum bottle (m)
g	Gravitational acceleration (g = 9.8 m/s^2)
β	Thermal expansion coefficient
δ	Thickness of air gap (mm)
T_t	Temperature of skeleton of the logging tool (K)
T_f	Temperature of inner wall of vacuum bottle (K)
Ra	Rayleigh number
Pr	Prandtl number
α_{air}	Thermal diffusion coefficient of air (m^2/s)
ν	Kinematic viscosity of the fluid (m^2/s)
$q_{solid,i}$	Heat flow of Contact solid thermal conduction between two adjacent spacer layers (W/m^2)
$q_{total,i}$	Total heat transfer between the i$_{th}$ and (i + 1)$_{th}$ reflective screens (W/m^2)
T_{air}	The temperature of air (K)
A	Surface area (m^2)
Q_c	Convective heat transfer through air (W)
Q_r	Radiative heat transfer through air (W)
ε_t	Surface emissivity of skeleton of the logging tool
ε_f	Surface emissivity of inner wall of vacuum bottle
h_{com}	Comsite convective heat transfer coefficient (W/(m^2·K))
k_{eff_air}	Equivalent thermal conductivity of air (W/(m·K))
k	Thermal conductivity (W/(m·K))
t	Time (s)
ρ	Density (kg/m^3)
c	Specific heat capacity (kJ/(kg·K))
L_m	Latent heat (kJ/kg)
c_{eff}	Equivalent heat capacity of PCM (kJ/(kg·K))
θ	Volume fraction of liquid PCM
h_L	Average convective heat transfer coefficient (W/(m^2·K))
r_h	Radius of the wellbore wall (m)
r_t	Radius of the logging tool (m)
U	Velocity of the logging tool (m/s)
L	Length of the logging tool (m)
α_{mud}	Thermal diffusion coefficient of mud (m^2/s)

Subscripts

i	Layer i
$i + 1$	Layer i + 1
PCM-S	Solid PCM
PCM-L	Liquid PCM

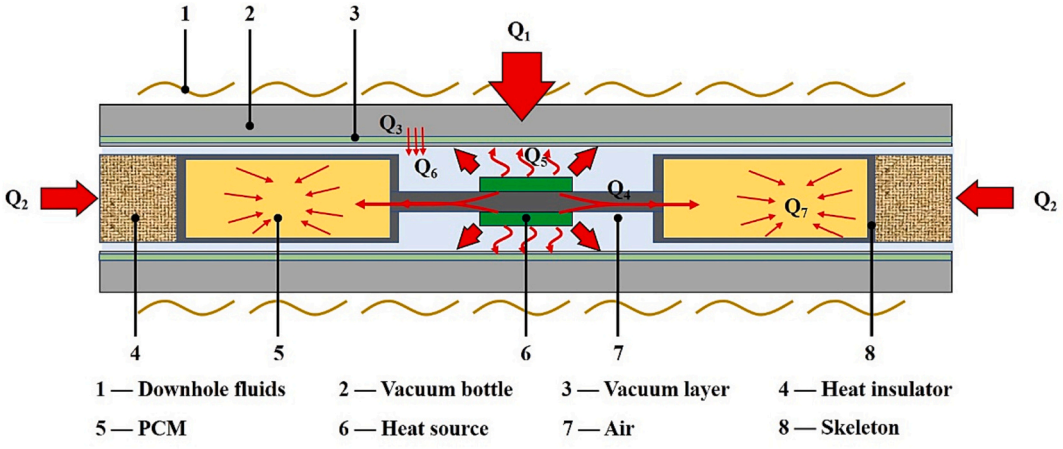

Fig. 1. The heat transfer process of PTMSs for logging tools.

temperature downhole thermoelectric cooling system. The system can cool the temperature of downhole electronic devices to about 130 °C at an ambient temperature of 160 °C. Soprani et al. [18] optimized a downhole thermoelectric cooling system by combining topology optimization and thermal simulation. A prototype was developed and operated continuously at 200 °C for 200 h, keeping the temperature of the 1 W electronics below 170 °C. Sinha et al. [19] proposed an active thermal management system with a combination of liquid cooling and thermoelectric coolers to enhance the heat exchange between the cold surface of the thermoelectric cooler and the downhole electronics. However, the COP of the thermoelectric cooler was generally low, with a small cooling power and insufficient high-temperature resistance, thus limiting the wide application in logging tools. In addition, thermoacoustic refrigeration [20] and Stirling refrigeration [21–23] were also restricted by the high-temperature reliability issues.

Comparatively, PTMS was widely used in oil logging due to its high reliability and convenience [24,25]. Fig. 1 shows the basic principle of PTMS for logging tools. On the one hand, a vacuum bottle combined with two heat insulators was employed to reduce the heat intrusion from a harsh external environment [26]. On the other hand, the heat generated by the electronics was transferred out immediately and stored in phase change materials (PCMs) [27]. Therefore, the heat transfer process in PTMS was complex, involving thermal conduction, thermal radiation, thermal convection, and phase change heat transfer. In order to meet the design requirements of PTMS according to different application scenarios, a numerical model of PTMS was essential to develop to investigate the heat transfer process and mechanism internal.

Several numerical models for PTMS have been proposed in previous studies to simulate the thermal performance under different conditions. Rafie [28] proposed a 1D numerical model considering heat conduction and thermal radiation, and the temperature rise within the system was obtained. Zhang et al. [29] established a 2D numerical model and analyzed the effects of different parameters. Shang et al. [30] developed a 2D axisymmetric model to derive the temperature cloud of the PTMS. Lan et al. [31] proposed a simplified 3D numerical model for PTMS with multiple heat sources by neglecting convective and radiative heat transfer. The relative error between the simulated results and experimental results was within 10%. Sur et al. [32] presented transient thermal models considering heat conduction and thermal convection. The calculated temperature was compared with experimental data, and the relative error was less than 8%. The numerical results were quickly obtained through the above numerical models due to the neglect of some heat transfer processes. Based on previous studies, Peng et al. [33] proposed a numerical mode of PTMS coupling all heat transfer modes to obtain more accurate numerical results. The average error between simulation and experiment was only 3.02 °C with a maximum relative error of 4.71%. However, the computational efficiency was pretty low due to the complex heat transfer process. Therefore, more efficient method was urgently needed to reduce the computation time while ensuring the computational accuracy. Furthermore, the vacuum layer was empirically determined to be equivalent to a solid layer with very low thermal conductivity in previous investigations, and the actual heat transfer process internal was not taken into account. Therefore, it is essential to investigate the heat transfer process in the vacuum bottle accurately and calculate the equivalent thermal conductivity of the vacuum layer theoretically.

This paper proposed a numerical model based on the equivalent thermal conductivity method to ensure the computational accuracy and efficiency simultaneously. Firstly, the equivalent thermal conductivity of the vacuum layer was determined by theoretical calculation. Subsequently, the convective and radiative heat transfer inside the vacuum bottle was equated to the thermal conductivity of air as a function of temperature. Finally, the experimental test was conducted to validate the effectiveness of the equivalent thermal conductivity method. In addition, the computational time and accuracy of the proposed numerical model were compared with previous studies.

2. Equivalent thermal conductivity method

2.1. Equivalence of heat transfer in the vacuum layer

Fig. 2 shows the schematic of the vacuum bottle, which consists of an inner and outer metal shell and a vacuum layer with multi-layer reflective screen. The performance of the vacuum layer directly determines the thermal insulation capacity of the bottle [34]. On the one hand, the thermal convection and thermal conduction of the gas in the vacuum layer can be significantly reduced due to high vacuum. On the other hand, the multi-layer reflective screens with high reflectivity are inserted into the vacuum layer to reduce the radiative heat transfer between the hot side and the cold side. In addition, the spacers with low thermal conductivity are inserted between the reflective screens to prevent solid contact thermal conduction. Therefore, the heat transfer between the hot and cold sides of the vacuum layer could be significantly reduced. However, there are still three forms of heat exchange within the vacuum layer, including thermal radiation between the reflective screen, thermal conduction of residual gas, and thermal conduction of solid contact between the spacer and the reflective screen.

Traditional numerical simulation is difficult to realize due to the complex heat transfer process. Therefore, the vacuum layer was regarded as a solid layer with very low thermal conductivity through the equivalent thermal conductivity method. Briefly, the equivalent calculation is performed by layer-by-layer model [35,36]. The single-layer reflective screen is taken as the research object in this model. The radiative heat transfer between neighboring reflective screens, the residual gas heat conduction, and the solid contact heat conduction are calculated iteratively based on the assumption of constant total heat flow between any two reflective screens. The total heat flow of the vacuum layer is obtained, and the equivalent thermal conductivity of the vacuum layer is calculated based on Fourier's law of thermal conduction.

The heat flow of radiative heat transfer between neighboring reflective screens can be expressed as [37]:

$$q_{radiation,i} = \frac{\sigma\left(T_{i+1}^4 - T_i^4\right)}{\frac{1}{\varepsilon_i} + \frac{1}{\varepsilon_{i+1}} - 1} \tag{1}$$

The heat flow of thermal conduction of the residual gas between two adjacent layers can be expressed as [38]:

$$q_{gas,i} = \frac{\gamma + 1}{\gamma - 1}\sqrt{\frac{\mathrm{R}}{8\pi \mathrm{M}T}} \cdot P \cdot B \cdot (T_{i+1} - T_i) \tag{2}$$

The heat flow of contact solid thermal conduction between two adjacent spacer layers can be expressed as [39]:

$$q_{solid,i} = \frac{\mathrm{C}fk_{spacer}}{D_i}(T_{i+1} - T_i) \tag{3}$$

k_{spacer} is the thermal conductivity of the spacer, which can be expressed as [35]:

$$k_{spacer} = 0.017 + 7 \times 10^{-6} \times \left(800 - \frac{T_{i+1} + T_i}{2}\right) + 0.0228ln\left(\frac{T_{i+1} + T_i}{2}\right) \tag{4}$$

The total heat flow between the i_{th} and $(i+1)_{th}$ reflective screens can be expressed as:

$$q_{\mathrm{total},i} = \frac{\sigma\left(T_{i+1}^4 - T_i^4\right)}{\frac{1}{\varepsilon_i} + \frac{1}{\varepsilon_{i+1}} - 1} + \frac{\gamma + 1}{\gamma - 1}\sqrt{\frac{\mathrm{R}}{8\pi \mathrm{M}T}} \cdot P \cdot B \cdot (T_{i+1} - T_i) + \frac{\mathrm{C}fk_{spacer}}{D_i}(T_{i+1} - T_i) \tag{5}$$

The total heat flow of the vacuum layer is consistent with the heat flow between any two reflective screens, and the equivalent thermal conductivity of the vacuum layer can be obtained according to Fourier's law of thermal conduction:

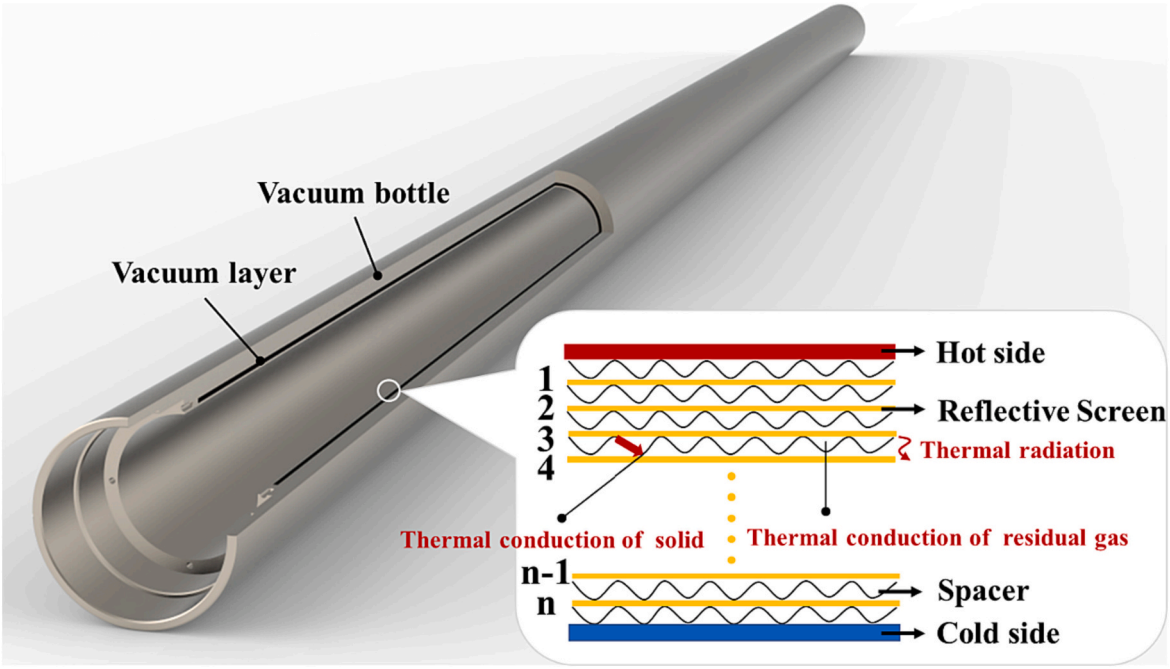

Fig. 2. The schematic of the vacuum bottle in logging tool.

$$k_{eff\_vacuum} = \frac{q_{total,i} \cdot \delta_{vacuum}}{(T_h - T_c)} \tag{6}$$

For an industrial metal vacuum bottle, the thickness of the vacuum layer is 3 mm with a vacuum degree of 10^{-3} Pa. The temperature of the hot and the cold side are 205 °C and 20 °C, respectively. The number of reflective screen layers is 10, and the emissivity of the reflective screen is 0.1. The temperature distribution and heat flow in the vacuum layer can be derived from Eqs. (1)–(5). Fig. 3(a) shows the temperature distribution in different reflective screen positions. The temperature of the reflective screen is not linearly related to its location. The temperature gradient of the reflective screen near the cold side is greater than that near the hot side. The reason is that near the hot side, the temperature of the reflective screen is high with strong radiation capacity, and the temperature difference between neighboring reflective screens is small under a certain heat flow. Fig. 3(b) reflects the heat flow between neighboring reflective screens versus the position of the reflective screen. The percentage of thermal radiation is much higher than the other two modes of heat transfer, which indicates that radiant heat transfer is the main mode of the vacuum layer in a high-temperature well. The total heat transfer is 1.378 × 10^2 W/m^2, and the percentages of thermal radiation, residual gas heat transfer, and solid contact heat transfer are 98.15%, 0.12%, and 1.73%, respectively.

Fig. 4 illustrates the influence of different absolute interlayer pressures on the thermal insulation performance of the vacuum layer. When the absolute pressure of the vacuum layer is lower than 10^{-2} Pa, the equivalent thermal conductivity and heat flow of the vacuum layer remain almost stable with the improvement of the vacuum degree, indicating that the thermal conduction of the residual gas accounts for a

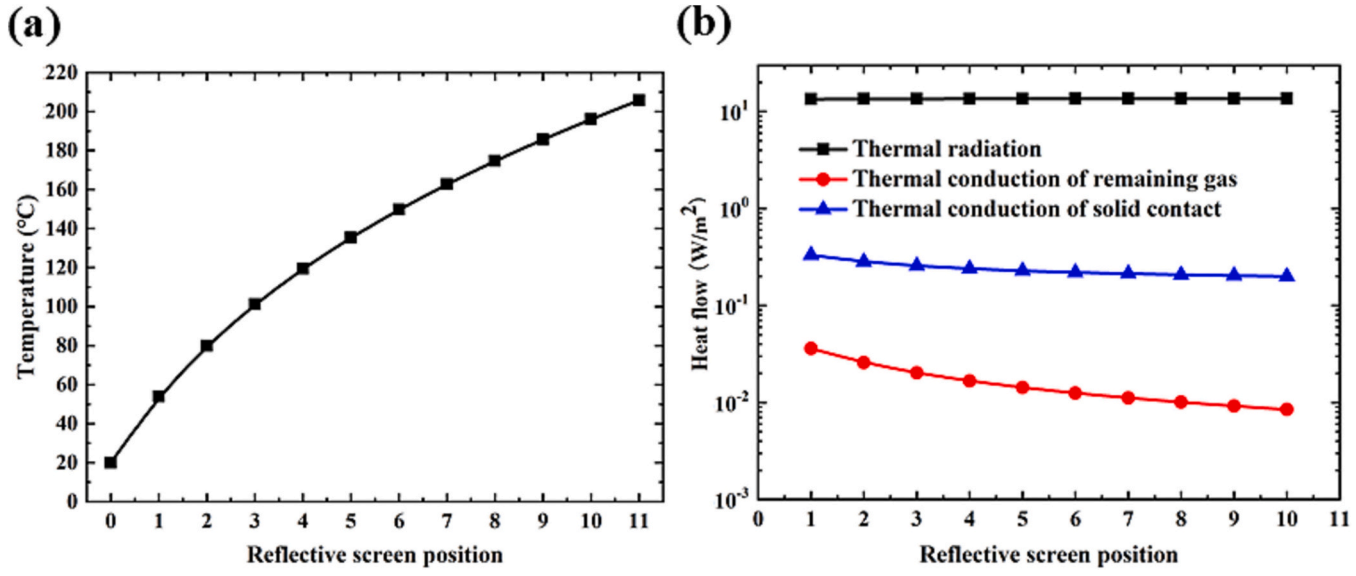

Fig. 3. The temperature distribution and heat flow in the vacuum layer. (a) temperature distribution in different reflective screen positions; (b) heat flow between neighboring reflective screens versus reflective screen positions.

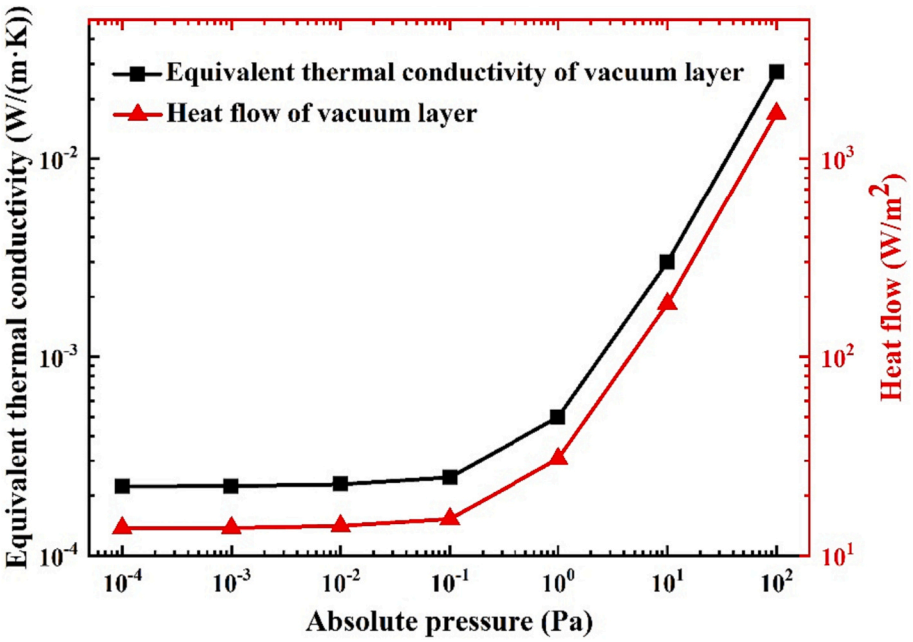

Fig. 4. The variation of equivalent thermal conductivity and heat flow of vacuum layer with absolute pressure.

very small percentage of heat transfer under the high vacuum degree. When the absolute pressure exceeds 10^{-1} Pa, the equivalent thermal conductivity and heat flux of the vacuum layer increase exponentially with the absolute interlayer pressure. This indicates that with the gradual loss of vacuum, the thermal conductivity of the residual gas gradually occupies a dominant position. When the absolute pressure is 100 Pa, the equivalent thermal conductivity of the vacuum adiabatic layer is 2.7×10^{-2} W/(m·K). The heat flow is 1.6922×10^{3} W/m^2, which is close to the effect of heat conduction of air. For the vacuum bottle of the actual logging tool, the absolute pressure between the layers is usually up to 10^{-3} Pa. In this case, the equivalent thermal conductivity of the vacuum layer is 2×10^{-4} W/(m·K), and the heat flow is 1.378×10^{2} W/m^2. Therefore, the vacuum layer of the vacuum bottle is treated as a solid layer with the equivalent thermal conductivity of 2×10^{-4} W/(m·K) in the subsequent numerical simulations.

2.2. Equivalence of thermal convection and radiation inside the vacuum bottle

The heat transfer modes inside the vacuum bottle include solid thermal conduction, convective heat exchange of air, radiant heat exchange between different surfaces, and phase change thermal storage. The previous numerical model considers multiple heat transfer modes with high accuracy, but the computational time is too long [33]. To improve the computational efficiency inside the logging tool, a heat transfer model of the logging tool is proposed in this paper based on the equivalent thermal conductivity method. The natural convective and radiative heat exchange inside the vacuum bottle is equivalent to the composite thermal conductivity of the air according to a certain criterion. Therefore, a transient heat transfer problem containing thermal conduction-convection-radiation can be converted into solid transient thermal conduction.

Fig. 5 shows the heat transfer schematic inside the logging tool based on the equivalent thermal conductivity method. The air gap of thickness δ exists between the skeleton with radius R_t and the inner wall of the vacuum bottle with radius R_f, where $\delta = R_f - R_t$. Natural convective and radiative heat transfer occurs on the surface of the skeleton with temperature T_t and the inner wall of the vacuum bottle with temperature T_f. The convective and radiative heat transfer are expressed as Q_c and Q_r, respectively. The convective heat transfer inside the logging tool occurs

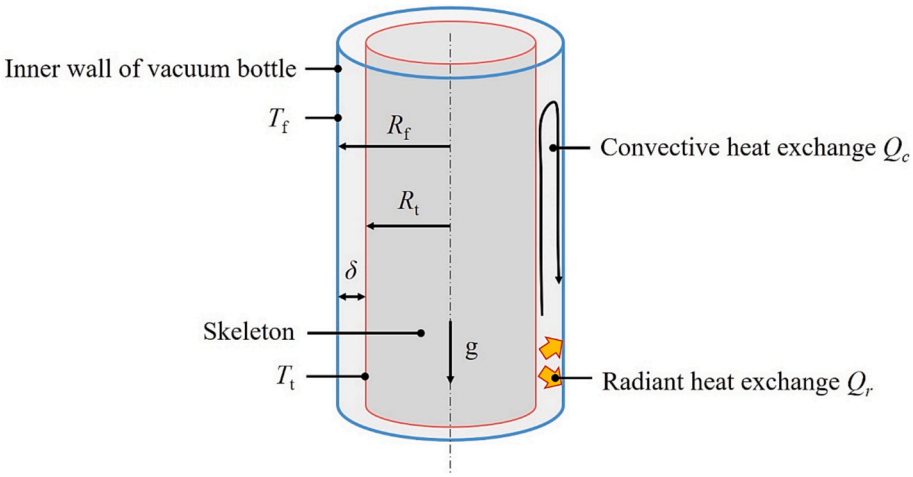

Fig. 5. The heat transfer schematic inside the logging tool based on the equivalent thermal conductivity method.

in the annular space, and the angular coefficient between the skeleton and the vacuum bottle can be considered as 1.

The natural convection heat transfer coefficient of the annular space can be expressed [40]:

$$h_c = \begin{cases} \dfrac{k_{\text{air}}}{R_t ln(R_f/R_t)} & (Ra \le 6000) \\ \dfrac{0.13 k_{\text{air}} Ra^{0.25}}{R_t ln(R_f/R_t)} & (6000 < Ra \le 5\times10^4) \\ \dfrac{0.049 k_{\text{air}} Ra^{1/3} Pr^{0.074}}{R_t ln(R_f/R_t)} & (5\times10^4 < Ra < 7.17\times10^8) \end{cases} \quad (7)$$

The Rayleigh number Ra can be expressed as:

$$Ra = \frac{g\beta(T_t - T_f)\delta^3}{\nu\alpha} \quad (8)$$

The coefficient of thermal expansion β can be expressed as:

$$\beta = \frac{1}{T_{\text{air}}} \quad (9)$$

The convective heat transfer in the annular space gap can be expressed as:

$$Q_c = \begin{cases} \dfrac{k_{\text{air}} A(T_t - T_f)}{R_t ln(R_f/R_t)} & (Ra \le 6000) \\ \dfrac{0.13 k_{\text{air}} Ra^{0.25} A(T_t - T_f)}{R_t ln(R_f/R_t)} & (6000 < Ra \le 5\times10^4) \\ \dfrac{0.049 k_{\text{air}} Ra^{1/3} Pr^{0.074} A(T_t - T_f)}{R_t ln(R_f/R_t)} & (5\times10^4 < Ra < 7.17\times10^8) \end{cases} \quad (10)$$

Based on the Stefan-Boltzmann law, the amount of radiative heat transfer can be expressed as:

$$Q_r = \frac{A\sigma(T_t^4 - T_f^4)}{\frac{1}{\varepsilon_t} + \frac{R_t}{R_f}\left(\frac{1}{\varepsilon_f} - 1\right)} \quad (11)$$

The composite heat transfer coefficient for the annular space gap can be expressed as:

$$h_{com} = \frac{Q_c + Q_r}{A(T_t - T_f)} \quad (12)$$

The equivalent thermal conductivity of the air can be expressed as:

$$k_{eff\_air} = k_{air} + h_{com} \cdot R_t \cdot ln(R_f/R_t) \quad (13)$$

Through the above steps, the equivalent thermal conductivity of the air in the annular space gap can be obtained, which takes into account the natural convection and thermal radiation simultaneously. Therefore, the complex heat transfer process including thermal conduction-convection-radiation can be simplified into a solid heat conduction process. It is conducive to the saving of computational resources and accelerating the speed of computation. It is worth noting that this equivalent thermal conductivity method is universal for all logging tools due to their similar structures.

3. Numerical model

3.1. Structure of the logging tool

Fig. 6 shows the structure of the PTMS for the logging tool, which is composed of a vacuum bottle, two heat insulators, two PCMs, and a metal skeleton. A vacuum bottle combined with two heat insulators is adopted to prevent heat intrusion from a high-temperature downhole environment. The vacuum layer in the bottle can greatly reduce radial

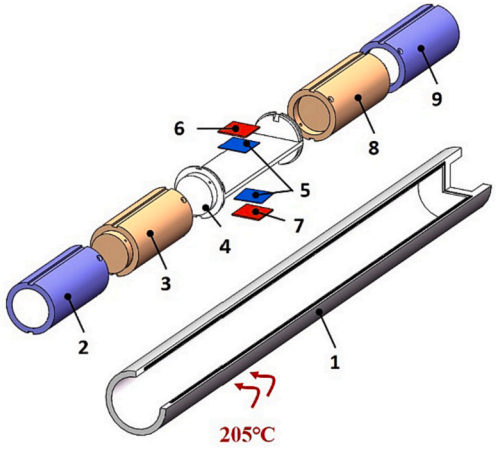

1 Vacuum bottle 2 Heat insulator 1 3 PCM 1
4 Metal skeleton 5 TIM 6 Heat source 1(20W)
7 Heat source 2(10W) 8 PCM 2 9 Heat insulator 2

Fig. 6. The structure of the PTMS for the logging tool.

heat transfer from the environment due to the high vacuum. The heat insulators are composed of materials with low thermal conductivity such as polytetrafluoroethylene and aluminum silicate wool, to decrease axial heat transfer. The outer and inner diameters of the vacuum bottle are 90 mm and 73 mm, respectively, with a vacuum layer thickness of 3 mm. Heat source 1 (20 W) and heat source 2 (10 W) are mounted on a metal skeleton via thermal interface material (TIM). The PCMs are located near the metal skeleton to quickly absorb the heat generated by heat sources. The diameter of the PCMs, metal skeleton, and thermal insulators are both 72 mm. Therefore, natural convective heat transfer and radiative heat transfer occur on both high-temperature and low-temperature surfaces of the annular space gap. In addition, forced convection heat transfer between the high-temperature and the outer wall surface of the vacuum bottle happens during the operation of the logging tool.

3.2. Heat transfer model of PTMS

The complex heat transfer process of the vacuum layer is treated as a solid heat transfer process with a thermal conductivity of 2×10^{-4} W/(m·K) according to the theoretical calculation. The thermal convection and radiation inside the vacuum bottle are equivalent to the thermal conductivity of air, which varies with temperature and time. In addition, some reasonable assumptions are made as follows:

(1) The contact thermal resistance is smaller compared to other thermal resistances. Therefore, the contact thermal resistance between surfaces is ignored [31].
(2) Changes in the physical properties of materials with temperature are ignored except for air.
(3) Due to the high viscosity of the liquid PCM used, the natural convection effect of the PCM could be neglected.

Based on the above assumptions, the heat transfer process of the PTMS can be simplified to a nonstationary heat conduction, which can be expressed as:

$$\rho c \frac{\partial T}{\partial t} = \nabla(k\nabla T) + q \quad (14)$$

The equivalent heat capacity method is used to simulate the phase change process of the PCM [41], which can be expressed as:

$$c_{eff} = \begin{cases} c_{PCM-S} & (T < T_s) \\ \frac{1}{\rho}[(1-\theta)\cdot\rho_{PCM-S}\cdot c_{PCM-S} + \theta\cdot\rho_{PCM-L}\cdot c_{PCM-L}] + \frac{L_m}{T_l - T_s} & (T_s \le T \le T_l) \\ c_{PCM-L} & (T_l < T) \end{cases} \quad (15)$$

The equivalent density can be expressed as:

$$\rho_{PCM} = (1-\theta)\cdot\rho_{PCM-S} + \theta\cdot\rho_{PCM-L} \quad (16)$$

The equivalent thermal conductivity can be expressed as:

$$k_{PCM} = (1-\theta)\cdot k_{PCM-S} + \theta\cdot k_{PCM-L} \quad (17)$$

θ is a function of temperature. It can be expressed as:

$$\theta = \begin{cases} 0 & (T < T_s) \\ \frac{V_{PCM-L}}{V_{PCM-L} + V_{PCM-S}} & (T_s \le T \le T_l) \\ 1 & (T_l < T) \end{cases} \quad (18)$$

Convective heat transfer between the metal vacuum bottle and the high temperature environment, and the average convective heat transfer coefficient can be expressed as [42]

$$h_L = \frac{1}{L}\int_0^L h(x) = \frac{3k_{mud}}{4}\left[\frac{U}{45(r_h - r_t)^2\alpha_{mud}L}\right]^{\frac{1}{3}}\left[(11r_h - 5r_t)^{\frac{1}{3}} + \left(\frac{29r_h - 5r_t}{16}\right)^{\frac{1}{3}}\right] \quad (19)$$

3.3. Simulation setup

Numerical simulations were conducted by the software COMSOL. The controlling equation and the structure of the PTMS for the logging tool were first imported into the computational fluid dynamics (CFD) solver. Then, the tetrahedral mesh was generated, and the mesh of the air domain was locally refined. Subsequently, the materials and thermal properties of each component were defined as shown in Table 1. Notably, the vacuum layer of the vacuum bottle was equivalent to a solid layer with a thermal conductivity of 2×10^{-4} W/(m·K) based on the previous calculations. The Wood alloy was applied to store heat generated by electronics with a latent heat of 36.68 kJ/kg. Importantly, the equivalent thermal conductivity of air varied with temperature according to Eq. (13), which changes in real-time. The heat sources generated heat uniformly with the heating power of 10 W and 20 W, respectively. The outside surface temperature of the vacuum bottle was set to 205 °C with the convective heat exchange boundary condition. The initial temperature of all components was set to 20 °C.

A grid-independence analysis was conducted to avoid the influence of the grid number on the calculated results. Numerical models with grid numbers 50,516, 77,259, 148,701, and 402,411 were calculated as shown in Table 2. Considering the computational time and the accuracy, we finally chose the numerical model with a grid number of 148,701 for subsequent studies. The maximum and minimum grid size of chosen numerical model were 72 mm and 9 mm, respectively. Accuracy analysis according to time step was conducted, and the results were shown in Table 3. Finally, the whole transient heat transfer process of the logging tool was calculated for 6 h with an output time step of 10 min.

In addition, to verify that the proposed model was able to calculate accurately and quickly, numerical simulations using the previous models were also performed.

Table 2
Grid independent analysis.

Grid number	Temperature of heat source 1	Grid number	Temperature of heat source 1
50,516	163.28 °C	148,701	160.13 °C
77,259	161.56 °C	402,411	160.24 °C

4. Experimental validation

Experimental tests were conducted to verify the accuracy of the simulated results. Fig. 7 shows a schematic diagram of the experimental test platform, which is composed of a vacuum bottle, a thermal management skeleton, an oven, two DC power supplies, several thermocouples, and a data acquisition instrument. The heat source of the thermal management skeleton consisted of two ceramic heating plates (5 V/10 W or 12 V/20 W, 40 mm × 40 mm × 2 mm, Zhengzhou Xindeng Electrothermal Ceramics Ltd.), powered by two DC power supplies (MS-3010D, 0–30 V/10 A, Dongguan Meisheng Power Technology Ltd.). During the experiments, all heat sources were continuously operated at their rated power (10 W or 20 W). Seven thermocouples (K type, 2 × 0.3 mm, temperature measurement accuracy = ±0.4 °C) were used to collect the temperature data in the experiment. A data acquisition instrument (MIK-R6000F, temperature measurement accuracy 0.2% FS ± 1D, sampling frequency = 1 Hz, Hangzhou Mecon Automation Technology Ltd.) was adopted to record the temperature measurement signals. An oven (KH-1000 A, temperature range = 10–250 °C, accuracy = ±1 °C, Shanghai Hecheng Instrument Manufacturing Ltd.) was utilized to maintain the set initial temperature, regulated by a proportional–integral–derivative (PID) controller. Note that the two ceramic heating plates were adhered to the adapter by thermal silicone pads (LC120, 1 W/(m·K)). In addition, all contact surfaces were filled with thermal interface materials to reduce the heat transfer thermal resistance. The whole experiment was maintained for 6 h at an oven temperature set at 205 °C.

5. Results and discussion

5.1. Comparison with simulations and experiment

Fig. 8 compares the temperature field at the final moment of PTMS

Table 3
Time step independent analysis.

Output time step	Temperature of heat source 1	Output time step	Temperature of heat source 1
20 min	162.14 °C	5 min	160.02 °C
10 min	160.13 °C	1 min	160.16 °C

Table 1
Materials and thermal properties of the logging tool [33].

Name	Material	Thermal conductivity (W·m^{-1}·K^{-1})	Density (kg•m^{-3})	Heat capacity (J•kg^{-1}•K^{-1})
Vacuum bottle	Inconel 718	14.7	8240	436
Vacuum layer	Composite	2×10^{-4}	100	1200
Skeleton	Aluminum alloy 6061	167	2710	896
Heat sources	Ceramic	30	3960	850
PCM	Wood alloy	19.8	9657.9	166.7(s)184(l)
Insulator shell	Polytetrafluoroethylene	0.25	2200	1000
Insulator core	Aluminum Silicate wool	0.035	400	794.2

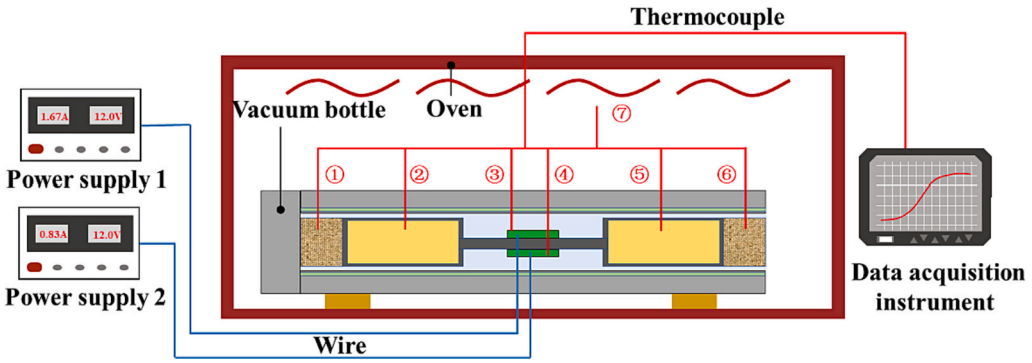

Fig. 7. Schematic diagram of the experimental test platform.

for the logging tool using three numerical models, including considering only thermal conduction, thermal conduction-convection-radiation, and the equivalent thermal conductivity method. It can be seen that the temperature field distributions of the three numerical models are subtle differences. If only thermal conduction is considered, the heat dissipation capacity of the outer surface of the heat source is insufficient. The temperature of the heat source is higher compared with the other two numerical models, reaching 164.22 °C. When considering natural convection and thermal radiation heat transfer in the cavity, the heat transfer ability of the outer surface of the heat source is enhanced. More heat generated from the heat source is emitted through natural convection and thermal radiation, so the final temperature of the heat source reaches 159.15 °C, which is 5.07 °C lower than the simulated result of only considering thermal conduction. The proposed model based on the equivalent thermal conductivity method mainly calculates the temperature distribution through the differential equation of thermal conductivity. However, the equivalent thermal conductivity of the air takes into account the thermal convection and thermal radiation heat transfer in the annulus. Therefore, the heat transfer capacity of the surface of the heat source is stronger than that of only considering the thermal conduction of the air. The final temperature of the heat source is decreased by 4.09 °C, reaching 160.13 °C. Compared to the simulated results that simultaneously consider the thermal-conduction-convection-radiation, the final temperature field of the proposed model is almost the same with the maximum temperature difference of the heat source only 0.98 °C.

Fig. 9 shows the heat sources' temperature of the three numerical results and the experimental results versus time. The results of the three numerical models have the same trend and are consistent with the experimental results. It can be seen that the temperature-rising curves of the equivalent thermal conductivity method and the method coupling thermal conduction-convection-radiation almost completely coincide with each other. The maximum absolute temperature error between the two methods in the final moment is only 1.02 °C, and the temperature-rising curves are closer to the experimental results. In contrast, the simulated results of only considering thermal conduction are close to those of the equivalent thermal conductivity method before 210 min. However, due to the enhancement of convective heat transfer and radiative heat transfer effects, the temperature difference between the two methods gradually increases during 210–360 min. On the whole, the numerical calculation results considering only thermal conduction have a large difference from the experimental results, and the maximum absolute temperature error is 8.61 °C. Whereas the numerical calculation results based on the equivalent thermal conductivity method have a maximum temperature error of less than 5 °C with the experimental results. This indicates that convective and radiative heat transfer can enhance heat dissipation of heat sources. The calculation results using equivalent thermal conductivity method match very well with the results of the numerical model coupling thermal conduction-convection-radiation, which indicates that the equivalent thermal conductivity method can well reflect the natural convective and radiative heat transfer in the logging tool.

5.2. *Equivalent thermal conductivity and heat flow*

To further explain the validity of the equivalent thermal conductivity method, the equivalent thermal conductivity of air and the heat flow on the outer surface of the heat source are both analyzed. Fig. 10 compares the thermal conductivity of air considering only thermal conduction and the equivalent thermal conductivity method. The thermal conductivity

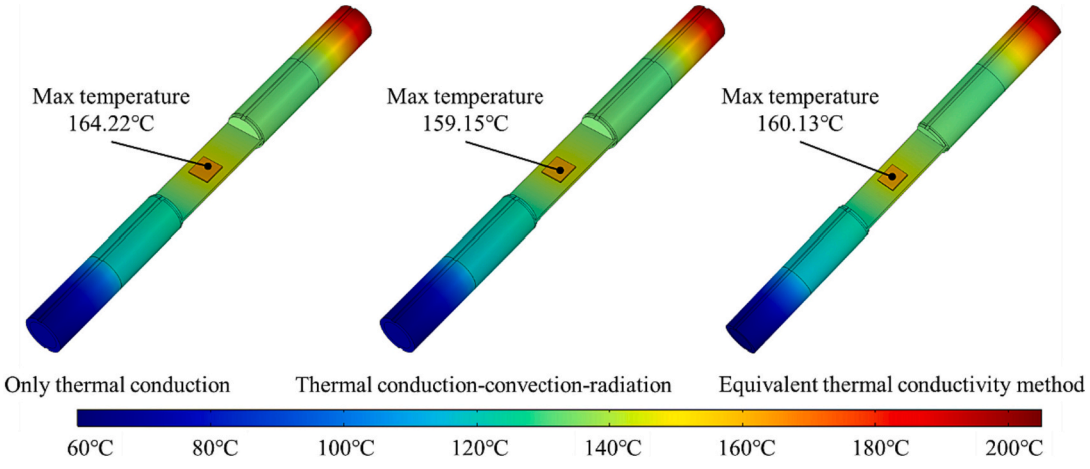

Fig. 8. The temperature field at the final moment of PTMS for the logging tool using three numerical models.

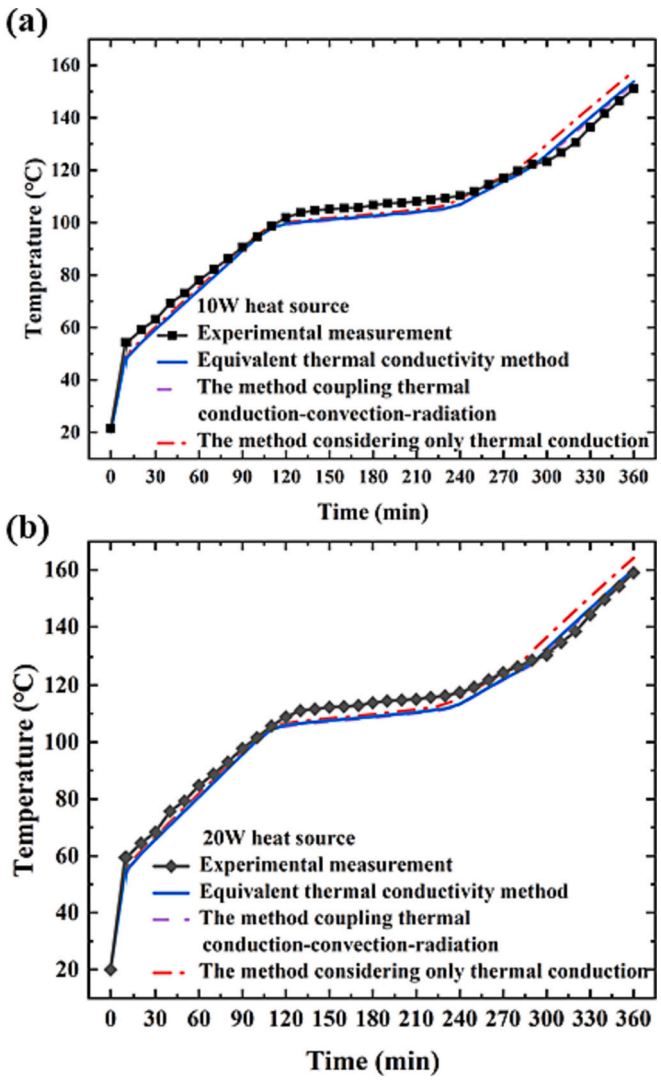

Fig. 9. The heat sources' temperature of the three numerical results and the experimental results versus time.

of air only considering thermal conduction gradually increases from 0.026 W/(m·K) to 0.034 W/(m·K) as the temperature increases. The thermal conductivity of air based on the equivalent thermal conductivity method is much higher than the intrinsic thermal conductivity of air, rising from 0.067 W/(m·K) to 0.170 W/(m·K). At the same time, the equivalent thermal conductivity of air as a function of temperature also remains constant during the phase transition interval. It can be explained that the temperature of the components surrounding the PCM remains almost constant due to the phase transition of the PCM. Overall, the average value of air equivalent thermal conductivity based on the equivalent thermal conductivity method is 0.127 W/(m·K), which is about 4.17 times the intrinsic average thermal conductivity of air.

The heat dissipation on the air side of the heat source of three numerical models are further compared as shown in Fig. 11. The heat dissipation on the outer surface of the heat source based on the equivalent thermal conductivity method is similar to that coupling thermal conduction-convection-radiation, whereas the heat dissipation considering only thermal conduction is significantly lower than the former two. The average heat transfer on the surface of the 20 W heat source based on the equivalent thermal conductivity method is 1.082 W, while the average heat transfer on the surface of the heat source coupling thermal conduction-convection-radiation and considering only thermal conduction are 1.130 W and 0.523 W, respectively. Similarly, the

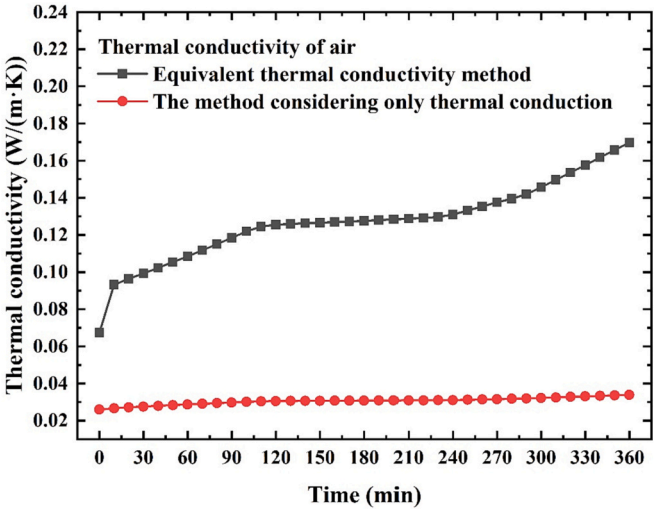

Fig. 10. The thermal conductivity of air for different numerical models.

average heat transfers on the surface of the 10 W heat source of the three models are 0.643 W, 0.682 W, and 0.296 W, respectively. In summary, it can be seen that the numerical model based on the equivalent thermal conductivity method effectively reflects the natural convective and radiative heat transfer of the air in the cavity of the vacuum bottle. The heat dissipation of the external surface of the heat source is improved by 1.1 times compared with the numerical model that only considers the thermal conduction of air.

5.3. Computational accuracy and efficiency

Finally, the computational efficiency of the proposed numerical model based on the equivalent thermal conductivity method is analyzed. Table 4 lists the computational accuracy and computational efficiency of the three numerical models. To control the variables, all the above cases are simulated under the same computer configuration (CPU: EPYC7742 × 2, memory: 128G, hard disk: 8 T). The number of cores used in the simulation are both 128 cores. The grid size and the grid numbers both remain the same in three models. In the model considering only thermal conduction, all the domains are calculated according to the thermal conduction differential equation. The computational accuracy is worst with an error of more than 5 °C. However, the computational time is the shortest, which is only 635 s. When the natural convection of air and thermal radiation are further considered, the continuity equation of the fluid and the momentum equation are needed to add to the thermal conduction differential equation. Furthermore, the angular coefficients and the surface-to-surface radiative heat transfer need to be calculated. Therefore, the complexity of equations is increased drastically, and the computational time increases to 29,296 s with the best accuracy. The numerical model based on the equivalent thermal conductivity method essentially uses the thermal conduction differential equation for the calculation of the full-domain nodes. However, the equivalent thermal conductivity of the air is coupled with the air temperature, the inner wall temperature of the vacuum bottle, and the surface temperature of the skeleton at the current moment. The equivalent thermal conductivity of air is updated continuously in the iterative process with time. Hence, the computational time of the numerical model based on the equivalent thermal conductivity method is bounded between the remaining two numerical models. The total simulation time consumed is 2964 s, which is only 10.1% of that of the numerical model coupling thermal conduction-convection-radiation. The computational accuracy of the proposed model is almost identical to the model coupling thermal conduction-convection-radiation. In summary, the proposed numerical model based on the equivalent thermal conductivity method can

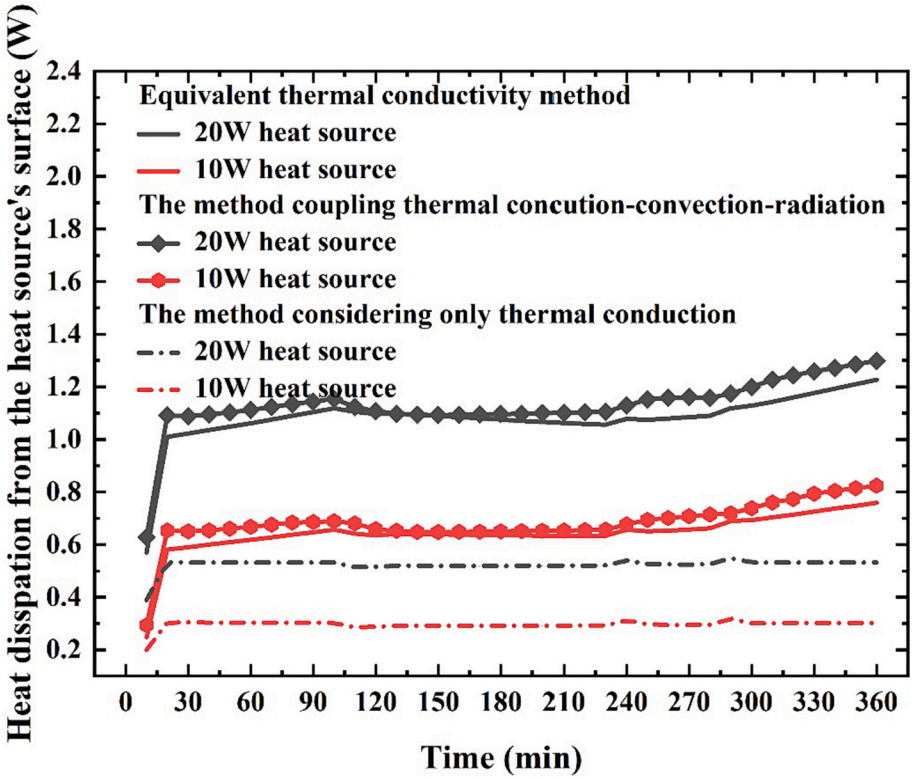

Fig. 11. The heat dissipation on the air side of the heat source for three numerical models.

Table 4
The computational accuracy and efficiency of the three numerical models.

Method	The final temperature of heat source 1(°C)	The final temperature of heat source 2(°C)	Computational time (s)
Considering only thermal conduction	164.22	157.70	635
Coupling thermal conduction-convection-radiation	159.15	152.75	29,296
Equivalent thermal conductivity method	160.13	153.77	2964
Experimental measurement	159.00	151.10	/

simultaneously consider computational accuracy and efficiency, which provides a more convenient method for the design of the thermal management system of logging tools.

6. Conclusions

In this paper, an improved numerical model based on the equivalent thermal conductivity method for downhole thermal management systems was proposed which possessed computational accuracy and efficiency simultaneously. The key conclusions in this study are as follows:

- Thermal radiation dominated during the heat transfer process in the vacuum layer, reaching to 98.15%. The equivalent thermal conductivity of the vacuum layer was calculated to be 0.0002 W/(m·K) under the actual working conditions.
- The convective and radiative heat transfer inside the vacuum bottle was equated to the temperature-dependent thermal conductivity of air, with the values ranging from 0.067 W/(m·K) to 0.170 W/(m·K).
- The accuracy of the proposed model was verified by experiment, and the deviation of electronics temperature was within 5 °C.
- Compared to the previous numerical models, the proposed numerical model achieved both computational accuracy and efficiency simultaneously. The computational time was drastically reduced from 29,296 s to 2964 s using the same configuration, which was expected to be widely used in the development of PTMS for logging tools.

CRediT authorship contribution statement

Jiale Peng: Writing – original draft, Validation, Methodology, Investigation, Formal analysis, Data curation, Conceptualization. **Wei Lan:** Methodology, Investigation, Conceptualization. **Chao Deng:** Methodology, Data curation. **Fulong Wei:** Investigation, Data curation. **Siqi Ding:** Validation. **Run Hu:** Funding acquisition. **Bofeng Shang:** Writing – review & editing, Supervision, Methodology, Funding acquisition. **Xiaobing Luo:** Supervision, Funding acquisition, Writing – review & editing.

Declaration of competing interest

The authors declare that they have no known competing financial interests or personal relationships that could have appeared to influence the work reported in this paper.

Data availability

Data will be made available on request.

Acknowledgment

This research is supported by the Open Fund Science and Technology on Thermal Energy and Power Laboratory (No. TPL2022B02), the

National Key R & D Project from the Ministry of Science and Technology of China (Grant No. 2022YFA1203100), and the Natural Science Foundation of Henan Province (Grant No. 222300420310).

References

[1] A. Kumar, A. Baldia, D. Rajput, S. Kateriya, V. Babu, K.K. Dubey, Multiomics and optobiotechnological approaches for the development of microalgal strain for production of aviation biofuel and biorefinery, Bioresour. Technol. 369 (2023) 128457.

[2] W. Li, D. Luo, J. Yuan, A new approach for the comprehensive grading of petroleum reserves in China: two natural gas examples, Energy 118 (2017) 914–926.

[3] Q. Lei, Y. Xu, Z. Yang, B. Cai, X. Wang, L. Zhou, H. Liu, M. Xu, L. Wang, S. Li, Progress and development directions of stimulation techniques for ultra-deep oil and gas reservoirs, Pet. Explor. Dev. 48 (2021) 221–231.

[4] S. Liu, Z. Li, B. Deng, W. Sun, Z. Li, Y. Ding, J. Song, J. Wu, Occurrence morphology of bitumen in Dengying formation deep and ultra-deep carbonate reservoirs of the Sichuan Basin and its indicating significance to oil and gas reservoirs, Nat. Gas Indust. B 9 (2022) 73–83.

[5] S. Soprani, A.J. Nørgaard, C. Nesgaard, K. Engelbrecht, Design and testing of a heat transfer sensor for well exploration tools, Appl. Therm. Eng. 141 (2018) 887–897.

[6] H. Wang, H. Huang, W. Bi, G. Ji, B. Zhou, L. Zhuo, Deep and ultra-deep oil and gas well drilling technologies: Progress and prospect, Nat. Gas Indust. B 9 (2022) 141–157.

[7] M.S. Khaled, N. Wang, P. Ashok, E. van Oort, Downhole heat management for drilling shallow and ultra-deep high enthalpy geothermal wells, Geothermics 107 (2023) 102604.

[8] J. Peng, W. Lan, F. Wei, C. Deng, X. Luo, Thermal management for high-power downhole electronics using liquid cooling and PCM under high temperature environment, in: 2022 IEEE 24th Electronics Packaging Technology Conference (EPTC), 2022, pp. 935–940.

[9] Y. Ma, B. Shang, R. Hu, X. Luo, Thermal management of downhole electronics cooling in oil & gas well logging at high temperature, in: 17th International Conference on Electronic Packaging Technology, 2016, pp. 623–627.

[10] J. Peng, W. Lan, Y. Wang, Y. Ma, X. Luo, Thermal management of the high-power electronics in high temperature downhole environment, in: 2020 IEEE 22nd Electronics Packaging Technology Conference (EPTC), 2021, pp. 369–375.

[11] S. Ma, S. Zhang, J. Wu, et al., Experimental study on active thermal protection for electronic devices used in deep− downhole− environment exploration, Energies 16 (3) (2023) 1231.

[12] Y. Lv, W. Chu, Q. Wang, Thermal management systems for electronics using in deep downhole environment: a review, Int. Commun. Heat Mass Transfer 139 (2022) 106450.

[13] S. Verma, Q. Elias, Thermal management of electronics used in downhole tools, in: SPE Annual Technical Conference and Exhibition, San Antonio, Texas, USA, 8–10 Oct. 2012 159737, OnePetro, 2012.

[14] B. Holbein, T. Schulenberg, Investigation on refrigerant transport by capillary effect with fleeces in an evaporator for a high temperature cooling machine, Int. J. Refrig. 93 (2018) 18–28.

[15] M. Wei, W. Cai, M. Xu, S. Deng, Active cooling system for downhole electronics in high-temperature environments, J. Therm. Sci. Eng. Appl. 14 (2022).

[16] A. Sinha, Y. Joshi, Application of thermoelectric-adsorption cooler for harsh environment electronics under varying heat load, J. Therm. Sci. Eng. Appl. 2 (2) (2010) 021004.

[17] R. Weerasinghe, T. Hughes, Analysis of thermal performance of geophonic downhole measuring tools; a numerical and experimental investigation, Appl. Therm. Eng. 137 (2018) 504–512.

[18] S. Soprani, J.H.K. Haertel, B.S. Lazarov, O. Sigmund, K. Engelbrecht, A design approach for integrating thermoelectric devices using topology optimization, Appl. Energy 176 (2016) 49–64.

[19] A. Sinha, Y.K. Joshi, Downhole electronics cooling using a thermoelectric device and heat exchanger arrangement, J. Electron. Packag. 133 (4) (2011) 041005.

[20] S. Tang, W. Gao, K. Liu, Design and numerical study of active cooling system of measurement while drilling for high temperature based on supersonic, Case Stud. Therm. Eng. 50 (2023) 103460.

[21] W. Gao, K. Liu, Y. Su, et al., Active cooling method for downhole systems in high temperature environment, in: SPE Western Regional Meeting, OnePetro, 2019.

[22] W. Gao, K. Liu, X. Dou, S. Tang, L. Zhang, Numerical investigation on cooling effect in the circuit cabin of active cooling system of measurement-while-drilling instrument based on split-Stirling retrigerator, Case Stud. Therm. Eng. 28 (2021) 101621.

[23] W. Gao, K. Liu, X. Dou, L. Zhang, S. Tang, Numerical investigation on heat transfer rate from the outside environment into the electronic compartment of the measurement-while-drilling tools, Heat Transfer 50 (6) (2021) 5835–5852.

[24] J. Zhang, W. Lan, C. Deng, F. Wei, X. Luo, Thermal Optimization of high-temperature downhole electronic devices, IEEE Trans. Compon. Packag. Manuf. Technol. 11 (2021) 1816–1823.

[25] J. He, Q. Wang, J. Wu, Y. Zhang, W. Chu, Hybrid thermal management strategy with PCM and insulation materials for pulsed-power source controller in extreme oil-well thermal environment, Appl. Therm. Eng. 214 (2022) 118864.

[26] F. Wei, C. Deng, J. Peng, et al., Thermal optimization of a logging tool used in high temperature downhole environment, in: 2022 IEEE International Power Electronics and Application Conference and Exposition (PEAC), IEEE, 2022, pp. 72–77.

[27] C. Deng, F. Wei, W. Lan, et al., Experimental and numerical investigation of low melting point alloy for downhole electronics at high temperature, in: 2022 IEEE International Power Electronics and Application Conference and Exposition (PEAC), IEEE, 2022, pp. 49–54.

[28] S. Rafie, Thermal management of downhole oil & gas logging sensors for hthp applications using nanoporous materials, in: Proceedings of 2nd Energy Nanotechnology International Conference 81, 2007, pp. S910–S931.

[29] X. Zhang, C. An, J. Zhang, Y. Zhang, Analysis of heat transfer performance of insulation casing filled with phase change material for downhole instruments, in: 30th International Ocean and Polar Engineering Conference, OnePetro, 2020, pp. 3120–3124.

[30] B. Shang, Y. Ma, R. Hu, C. Yuan, J. Hu, X. Luo, Passive thermal management system for downhole electronics in harsh thermal environments, Appl. Therm. Eng. 118 (2017) 593–599.

[31] W. Lan, J. Zhang, J. Peng, Y. Ma, S. Zhou, X. Luo, Distributed thermal management system for downhole electronics at high temperature, Appl. Therm. Eng. 180 (2020) 115853.

[32] A. Sur, B. Kouchmeshky, R. Satti, Thermal modeling of a wireline tool for ultra-high temperatures, in: Proceedings of the ASME 2014 4th Joint US-European Fluids Engineering Division Summer Meeting, ASME, 2014, p. 21851.

[33] J. Peng, W. Lan, F. Wei, C. Deng, B. Xie, X. Luo, A numerical model coupling multiple heat transfer modes to develop a passive thermal management system for logging tool, Appl. Therm. Eng. 223 (2023) 120011.

[34] J. Peng, Y. Wang, S. Ding, C. Deng, F. Wei, X. Luo, Rapid detection of the vacuum failure of logging tools based on the variation in equivalent thermal conductivity, Int. J. Therm. Sci. 188 (2023) 108245.

[35] Y. Huang, B. Wang, S. Zhou, J. Wu, G. Lei, P. Li, P. Sun, Modeling and experimental study on combination of foam and variable density multilayer insulation for cryogen storage, Energy 123 (2017) 487–498.

[36] S. Wu, J. Li, P. Ding, Z. Ouyang, Calculation and analysis of optimal layer density for variable density multilayer insulation based on layer by layer model and Lockheed equation, Cryogenics 132 (2023) 103699.

[37] M.F. Modest, S. Mazumder, Radiative Heat Transfer, Academic press, 2021.

[38] H. Wu, H. Tan, Inversion of interlayer pressure in high-vacuum multilayer insulation structures for cryogen storage using extreme learning machine, Appl. Sci. 13 (2023) 5779.

[39] W. Jiang, P. Sun, P. Li, Z. Zuo, Y. Huang, Transient thermal behavior of multi-layer insulation coupled with vapor cooled shield used for liquid hydrogen storage tank, Energy 231 (2021) 120859.

[40] F. Zhou, X. Zheng, Heat transfer in tubing-casing annulus during production process of geothermal systems, J. Earth Sci. 26 (1) (2015) 116–123.

[41] Y. Hu, R. Guo, P.K. Heiselberg, H. Johra, Modeling PCM phase change temperature and hysteresis in ventilation cooling and heating applications, Energies 13 (23) (2020) 6455.

[42] J. Peng, C. Deng, F. Wei, S. Ding, R. Hu, X. Luo, A hybrid thermal management system combining liquid cooling and phase change material for downhole electronics, J. Energ. Storage 72 (2023) 108610.